

Three-dimensional needle network model for dendritic growth with fluid flow

Thomas Isensee^{1,2}, Damien Turret¹

¹ *IMDEA Materials Institute, Getafe, 28906 Madrid, Spain*

² *Polytechnic University of Madrid, 28040 Madrid, Spain*

damien.turret@imdea.org

Abstract

We present a first implementation of the Dendritic Needle Network (DNN) model for dendritic crystal growth in three dimensions including convective transport in the melt. The numerical solving of the Navier-Stokes equations is performed with finite differences and is validated by comparison with a classical benchmark in fluid mechanics for unsteady flow. We compute the growth behavior of a single equiaxed crystal under a forced convective flow. As expected, the resulting dendrite morphology differs strongly from the case of the purely diffusive regime and from similar two-dimensional simulations. The resulting computationally efficient simulations open the way to studying mechanisms of microstructure selection in presence of fluid flow, using realistic alloys and process parameters.

1. Introduction

Dendritic microstructures are common in solidification-processed metals and alloys [1, 2]. Their morphology has crucial influence on the thermo-mechanical properties of these materials [3]. Dendritic patterns are shaped by the interaction of individual dendritic branches and hence arise from mechanisms on different length scales, i.e. phenomena on the scale of the microscopic solid-liquid interface, and macroscopic heat and solute transport. For decades, the aim to bridge scales has motivated the development of a wide range of multiscale simulations approaches, e.g. using dedicated formulations for enthalpy terms [4], volume-averaged conservation equations [5], cellular automata coupled with finite elements [6] or finite differences [7], or dynamics of grain envelopes [8], to name a few. Macroscopic heat and solute transport can be strongly influenced by advective currents. Since buoyancy can be caused by gravity [9–11], it is almost impossible to carry out solidification experiments in homogeneous conditions. Experiments with reduced gravity have provided important insight into the effect of buoyancy onto microstructure selection [12–14], however only at great expense, which is why the modeling of dendritic growth under fluid flow is of tremendous interest.

In contrast to growth in the purely diffusive regime, in the presence of fluid flow, growing crystals are asymmetric. The problem has been investigated analytically, e.g. using a diffusive boundary layer (“stagnant film”) around the dendrite [15–17], and computationally, e.g. with models that explicitly track the solid-liquid surface [18–20] or phase-field (PF) simu-

lations [21–26]. However, these models still require a reasonably accurate resolution of the dendrite tip morphology, which limits their use in the case of concentrated alloys that usually solidify with thin needle-like branches with a tip radius much lower than the scale of macroscopic transport of heat and solute in the melt.

To address this multiscale problem we developed a *dendritic needle network* (DNN) model, in which the dendrite branches are represented as thin paraboloids. The model quantitatively predicts the dynamics of individual branches in complex hierarchical networks during alloy solidification at a scale much larger than the diffusion length, and it is particularly adapted to solidification at low supersaturation, i.e. low Péclet number, when phase field simulations become prohibitively costly. The key computational advantage of the method comes from the fact that the numerical grid spacing can be chosen of the same order as the dendrite tip radius, which is typically one order of magnitude coarser than the requirement for quantitative phase-field simulations. This results in simulations faster by several orders of magnitude, with minimal loss in accuracy [27]. The DNN model, developed in two dimensions (2D) [28] and three dimensions (3D) [29], was already verified against classical theories and phase-field simulations of dendritic growth, and validated against directional solidification experiments in a predominantly diffusive transport regime [29–31]. A first incorporation of fluid flow in 2D was also achieved [32]. However, since flow patterns strongly differ in 2D and 3D, quantitative simulations require a 3D implementation. Here we present first results of the DNN model including fluid flow in 3D.

2. Model

2.1. Sharp-interface problem

Considering a binary alloy at a temperature $T = T_0$ below its liquidus temperature T_L , we introduce a dimensionless form of the solute concentration field c , i.e. the supersaturation

$$U := \frac{c_0 - c}{(1 - k)c_0} \quad (1)$$

with c_0 and k the liquid equilibrium concentration at $T = T_0$ and the interface solute partition coefficient, respectively. Neglecting diffusion in the solid phase, the solute concentration in the liquid close to the solid-liquid interface (e.g. within a diffusive boundary layer) follows

$$\partial_t U = D \nabla^2 U. \quad (2)$$

Solute mass conservation at the interface takes the form of a Stefan condition

$$\mathbf{v}_n = D \partial_n U|_i, \quad (3)$$

that relates the interface normal velocity \mathbf{v}_n to the normal solute concentration gradient $\partial_n U|_i$. Neglecting kinetic undercooling, the Gibbs-Thomson relation for interfacial equilibrium is

$$U_i = d_0 f_\gamma(\bar{\theta}) \kappa, \quad (4)$$

where κ is the interface curvature, $d_0 = \Gamma_{sl} / [|m|(1 - k)c_0]$ the solutal capillary length with the liquidus slope $m < 0$ and the Gibbs-Thomson coefficient Γ_{sl} . The anisotropy function $f_\gamma(\bar{\theta})$ represents the dependence of the interface stiffness $\gamma(\bar{\theta}) + \partial_{\bar{\theta}}^2 \gamma(\bar{\theta}) = \gamma_0 f_\gamma(\bar{\theta})$ upon the interface orientation $\bar{\theta}$, where $\gamma(\bar{\theta})$ is the excess free-energy of the solid-liquid interface and γ_0 is its average value [33, 34]. Eqs. (2) - (4) describe the sharp interface problem for a growing solid-liquid interface, combined with an imposed supersaturation

$$\Omega := \frac{c_0 - c_\infty}{(1 - k)c_0} \quad (5)$$

far away from the interface, with c_∞ the nominal solute concentration.

2.2. DNN model

The DNN model is designed to model solidification at low supersaturation, i.e. at a Péclet number $Pe = RV/(2D) \ll 1$, with R and V the dendrite tip radius and velocity, respectively, and D the liquid solutal diffusion coefficient. With a tip radius much smaller than the diffusion length $l_D = D/V$, conservation equations can be derived at different length scales, such that: (i) mass conservation on an intermediate scale between the tip radius R and the diffusion length, provide the product RV (or RV^2 in 2D),

and (ii) microscopic solvability theory at the scale of R prescribes the constant value of R^2V . The combination of those conditions, described below, enables to obtain the instantaneous growth conditions $R(t)$ and $V(t)$ for each dendritic tip.

2.3. Microscopic solvability condition at the scale of the dendrite tip

The well-established solvability theory [35–38] states that the sharp-interface problem described by eqs. (2) - (4) has a steady solution only if

$$R^2V = \frac{2Dd_0}{\sigma}, \quad (6)$$

where the selection parameter σ is uniquely determined by the strength of the interface crystalline anisotropy. The theory was confirmed using PF simulations [39–41], which even showed that the product R^2V relaxes to a constant very early during growth, while $R(t)$ and $V(t)$ still undergo significant variations [41]. Analytical [42] and phase-field [22, 24, 25] studies have also shown, that σ remains constant up to fluid velocities about one order of magnitude higher than the tip velocity. Thus, the DNN model considers eq. (6) to be valid at all times.

2.4. Conservation of solute on an intermediate scale

On a scale larger than the tip radius, dendritic branches appear sharp and curvature effects can be neglected, so that the equilibrium concentration $U = U_i \approx 0$ is assumed along the interface. Assuming a paraboloid with its tip at x_t and a cross section of radius $r_i(x) = \sqrt{(2R(x_t - x))}$ growing in a shape-preserving manner with velocity V , the mass conservation (eq. (3)) integrated over a contour Γ_0 that spans until a length a behind the tip (see figure 1) yields

$$D \int_{\Gamma_0} (\partial_n U) d\Gamma_0 = \int_0^{2\pi} \int_0^{r_a} V r dr d\theta = 2\pi a R V, \quad (7)$$

where r_a is the cross section of the paraboloid at $x = x_t - a$. By introducing the flux intensity factor (FIF)

$$\mathcal{F} := \frac{1}{2\pi a} \int \int_{\Gamma_0} (\partial_n U) d\Gamma_0, \quad (8)$$

the product RV can be expressed as

$$RV = D\mathcal{F}. \quad (9)$$

To integrate over Γ_0 , we use the divergence theorem and the assumption of a Laplacian field in a moving frame with velocity V , i.e. $D \nabla^2 U = -V \partial_x U$, yielding

$$\int \int_{\Gamma_0} (\partial_n^* U) dS = \int \int_{\Gamma_i} (\partial_n U) dS + \frac{V}{D} \int \int \int_{\Sigma_i} (\partial_x U) dV. \quad (10)$$

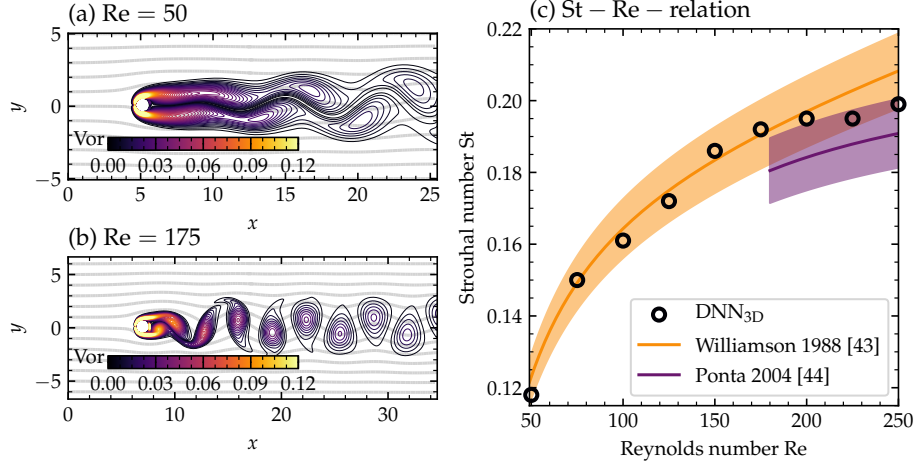


Figure 2: (a) and (b) Contour plots of the absolute value of the vorticity in a flow with $Re = 50$ and $Re = 175$, respectively, past a cylindrical obstacle with the maximum value shown in white and the minimum value in black. The gray streamlines indicate that the domain is large enough for the boundary conditions to not come into play. The cross section was taken in the center of the three dimensional domain. (c) Strouhal versus Reynolds number in comparison with universal laws from the literature, i.e. [43] for $49 < Re < 180$ and [44] for $Re \geq 180$. The shaded area indicates a 5% uncertainty margin.

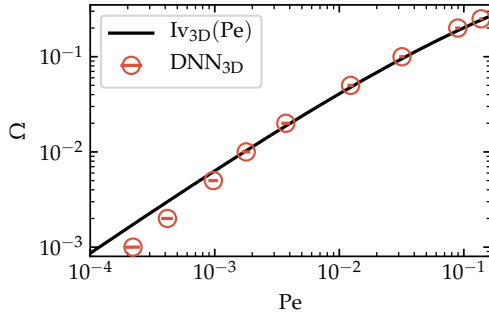


Figure 3: Imposed supersaturation Ω versus Péclet number Pe of a single isolated dendrite predicted by 3D DNN simulations in comparison with the analytical Ivantsov law $Iv_{3D}(Pe)$ [49]. The grid spacing Δx was chosen so that the diffusion length $l_D = 15\Delta x$. Each value is an average over a time range that covers several oscillations. The error bars correspond to the standard deviation.

4. Equiaxed crystal growth in a forced flow

4.1. Simulations

Finally, having independently verified the implementation of the Navier-Stokes equations and dendritic growth in the diffusive regime, we simulate the growth of equiaxed dendrites under forced flow. We perform simulations in both 2D and 3D for conditions close to those studied in 2D in [32]. We consider a model alloy of Schmidt number $Sc = \nu/D = 20$, with $\nu = \eta/\rho$ the kinematic viscosity, at a solute supersaturation $\Omega = 0.5$. We use a tip selection parameter $\sigma = 0.06$ in 2D and $\sigma = 0.04$ in 3D, which both correspond to a solid-liquid interface energy anisotropy of amplitude ≈ 0.01 for a one-sided model [37].

For the 3D simulation we use a domain with a size of $L_x \times L_y \times L_z = 51.0R_s \times 25.4R_s \times 25.4R_s$ with a grid spacing of $\Delta x = 0.1R_s$. An inflow with velocity

$(u_i, 0, 0)$ is imposed at the left boundary ($x = 0$), while the right boundary is set to allow free outflow, and the remaining boundaries hold free-slip conditions for the velocity (i.e. $v = \partial v / \partial y = 0$ in for y -boundaries and $w = \partial w / \partial z = 0$ for z -boundaries). Mirror symmetry conditions are applied for the diffusive field U at all boundaries. Exploiting the symmetry of the domain and the expected laminar flow, we initiate a single equiaxed grain along the the ($y = z = 0$) edge of the domain, centered at $(25.5R_s, 0, 0)$. The grain consists four branches, with directions $x+$, $x-$, $y+$, and $z+$, and initial radii and lengths of $0.4R_s$ and $2R_s$, respectively. For the 2D simulation, we use similar boundary conditions and grid spacing but with a size of $L_x \times L_y = 205R_s \times 102R_s$. The grain is generated at $(102R_s, 0)$.

For similar physical parameters, the expected steady state velocities V_s in 2D and 3D differ, such that the scaled inflow velocities u_i/V_s also differ. Combining microscopic solvability (6) with the definition of the Péclet number, $Pe = RV/(2D)$, one can write $V_s d_0/D = 2\sigma P_s^2$. For $\Omega = 0.5$, since the Péclet number is 0.1873 in 2D and 0.6101 in 3D, the steady growth velocity V_s in 3D is about 7 times higher than in 2D. The inflow velocity is set to $u_i = 0.0421/d_0$, which corresponds to $u_i/V_s = 10.0$ in 2D and $u_i/V_s = 1.41$ in 3D.

The total simulation time is chosen as $20R_s/V_s$, which was found to be sufficient to achieve steady-state growth. For both 2D and 3D simulations, the numerical parameters are $K_{\Delta t} = 0.6$, $\omega_{up} = 0.9$, $\omega_{SOR} = 1.7$ and $\bar{r}_{SOR} = 10^{-3}$ (see Ref. [32] for details). The FIF integration domain has a radius $r_{FIF} = 5\Delta x$. Side branches are generated every time a needle grows by $10R_s$.

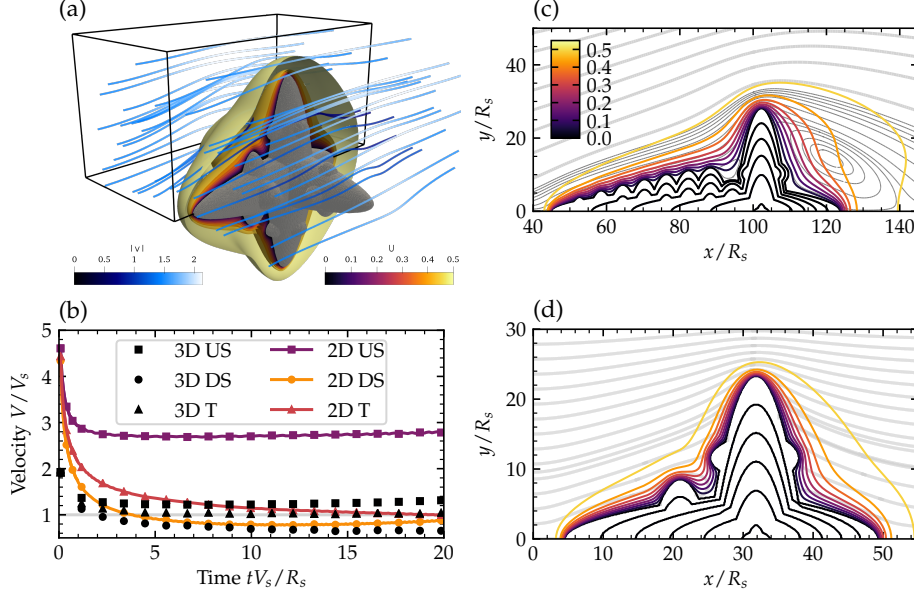


Figure 4: (a) Dendritic grain (gray) under forced flow predicted by the DNN model at a time $20R_s/V_s$. The iso-surfaces indicate the dimensionless solute field U from 0 to 0.5 with steps of 0.1 and the streamlines show the laminar flow around the crystal. (b) and (d) show the cross section along the fluid flow direction. The colored contour lines indicate the field U ; the black lines show the location of the solid-liquid interface at $tV_s/R_s = 0, 4, 8, 12, 16$, and 20 . The gray streamlines represent iso-values of the stream function. The plots do not show the complete simulation domain. Plot (b) shows a higher density of thinner streamlines close to the dendrite in order to highlight the convective vortices next to the downstream tip. (c) Velocities of the upstream, downstream and transverse tips over time. The values correspond to average values over a small time range in order to smoothen the curves.

4.2. Results

The 3D simulation was performed in under 20 h with a single Nvidia RTX 2080TI GPU, and the results are illustrated in Fig. 4. Fig. 4a shows the grain shape in the 3D simulation after a time $20R_s/V_s$, with iso-surface of the solute field and streamlines of the flow. Fig. 4b shows the evolution of the upstream (US), downstream (DS), and transverse (T) tips in both 2D and 3D simulations. Fig. 4c-d shows the interface, solute field, and streamlines in 2D (c) and along the ($z = 0$) plane in 3D (d).

Qualitatively, the effect of fluid flow on the tip velocities is similar, namely the upstream tip velocity is increased, the downstream tip velocity is decreased, and the steady transverse tip velocity is barely affected. However, the amount of change differs substantially between 2D and 3D simulations. The upstream velocity increase is much higher in 2D (about 3 times higher than the transverse tip velocity) than in 3D (increased by about 40%). This is not only due to the different scaling of V_s in 2D and 3D, but also to the resulting flow pattern. As already pointed out in previous studies [23–25, 50], in 3D the flow can easily pass by the transverse arm while in 2D the arm acts as a wall that the flow has to entirely go around. As a result, the flow velocities are overestimated in 2D, and flow patterns are also importantly affected.

An important consequence on the flow pattern is the formation of convective vortices around the downstream arm, which only appear in 2D. An outcome of these 2D vortices is that the downstream tip acceler-

ates as the vortices feed it solute, and hence the tip cannot reach a steady state. Meanwhile, in 3D, the downstream tip seems to reach a well-defined steady growth velocity.

5. Summary and outlook

We presented the first three-dimensional implementation of the Dendritic Needle Network (DNN) model for binary alloy isothermal solidification with fluid flow. The code implementation was validated for unsteady oscillatory flow past an obstacle, and verified for steady state growth in the diffusive regime. Then, we performed simulations of equiaxed growth of a single grain in a forced flow and compared results of 2D and 3D simulations. The results show that the growth dynamics significantly deviates from diffusive solidification. Furthermore, the acceleration of the upstream tip and deceleration of the downstream tip, differ significantly in the 2D and 3D cases, in agreement with previous studies [23, 24]. These results further highlight the importance of 3D simulations in order to produce results that can be compared to experiments or solidification processes on a quantitative basis.

In the future, we expected the DNN model to provide computationally efficient and spatially extended simulations of solidification in a low Péclet number regime that remains challenging to established simulation methods such as phase-field. This should allow exploring the mechanisms of microstructure selection

at the scale of thousands of dendrites [29, 31]. On-going and upcoming developments from this work include: quantitative comparison to phase field simulations [23, 24], study of the effect of the relative orientations of crystal and flow [50, 51], and the extension to directional solidification conditions [28, 29] in order to study, for instance, the selection of dendritic spacings in the presence of micro- or hyper-gravity conditions [52, 53], or the selection of grain boundary orientations during columnar grain growth competition [54, 55].

Acknowledgements

This work was supported by the European Unions Horizon 2020 research and innovation programme through DTs Marie Skłodowska-Curie Individual Fellowship (Grant Agreement 842795).

References

- [1] J.S. Langer. Instabilities and pattern formation in crystal growth. *Rev. Mod. Phys.*, 52(1):1 – 28, 1980.
- [2] R. Trivedi and W. Kurz. Dendritic growth. *International Materials Reviews*, 39(2):49–74, 1994.
- [3] J. A. Dantzig and M. Rappaz. *Solidification*. Materials. EPFL Press, Lausanne, Switzerland, 2009.
- [4] Vaughan R Voller and C Prakash. A fixed grid numerical modelling methodology for convection-diffusion mushy region phase-change problems. *International Journal of Heat and Mass Transfer*, 30(8):1709–1719, 1987.
- [5] CY Wang and Ch Beckermann. Equiaxed dendritic solidification with convection: Part i. multiscale/multiphase modeling. *Metallurgical and materials transactions A*, 27(9):2754–2764, 1996.
- [6] Ch-A Gandin, J-L Desbiolles, Michel Rappaz, and Ph Thevoz. A three-dimensional cellular automaton-finite element model for the prediction of solidification grain structures. *Metallurgical and Materials Transactions A*, 30(12):3153–3165, 1999.
- [7] W Wang, Peter D Lee, and M. Mclean. A model of solidification microstructures in nickel-based superalloys: predicting primary dendrite spacing selection. *Acta materialia*, 51(10):2971–2987, 2003.
- [8] Ingo Steinbach, Christoph Beckermann, B Kauerauf, Q Li, and J Guo. Three-dimensional modeling of equiaxed dendritic growth on a mesoscopic scale. *Acta Materialia*, 47(3):971–982, 1999.
- [9] R. Mehrabian, M. Keane, and M.C. Flemings. Interdendritic fluid flow and macrosegregation; influence of gravity. *Metallurgical Transactions*, 1:1209–1220, 1970.
- [10] H. Nguyen-Thi, B. Billia, and H. Jamgotchian. Influence of thermosolutal convection on the solidification front during upwards solidification. *Journal of Fluid Mechanics*, 204:581 – 597, 1989.
- [11] M.D. Dupouy, D. Camel, and J.J. Favier. Natural convection in directional dendritic solidification of metallic alloys. macroscopic effects. *Acta Metallurgica*, 37(4):1143 – 1157, 1989.
- [12] M.E. Glicksmann, M.B. Koss, and E.A. Winsa. Dendritic growth velocities in microgravity. *Phys. Rev. Lett.*, 73(4):573–576, 1994.
- [13] H. Nguyen-Thi, Y. Dabo, B. Drevet, M.D. Dupouy, D. Camel, B. Billia, J.D. Hunt, and A. Chilton. Directional solidification of al1.5wt% ni alloys under diffusion transport in space and fluid-flow localisation on earth. *Journal of Crystal Growth*, 281(2):654 – 668, 2005.
- [14] H. Nguyen-Thi, G. Reinhart, and B. Billia. On the interest of microgravity experimentation for studying convective effects during the directional solidification of metal alloys. *Comptes Rendus Mcanique*, 345(1):66 – 77, 2017. Basic and applied researches in microgravity A tribute to Bernard Zappolis contribution.
- [15] B. Cantor and A. Vogel. Dendritic solidification and fluid flow. *Journal of Crystal Growth*, 41(1):109 – 123, 1977.
- [16] Q. Li and C. Beckermann. Modeling of free dendritic growth of succinonitrileacetone alloys with thermosolutal melt convection. *Journal of Crystal Growth*, 236(1):482 – 498, 2002.
- [17] R.F. Sekerka, S.R. Coriell, and G.B. McFadden. Stagnant film model of the effect of natural convection on the dendrite operating state. *Journal of Crystal Growth*, 154(3):370 – 376, 1995.
- [18] H.S. Udaykumar, S. Marella, and S. Krishnan. Sharp-interface simulation of dendritic growth with convection: benchmarks. *International Journal of Heat and Mass Transfer*, 46(14):2615 – 2627, 2003.
- [19] N. Al-Rawahi and G. Tryggvason. Numerical simulation of dendritic solidification with convection: Two-dimensional geometry. *Journal of Computational Physics*, 180(2):471 – 496, 2002.
- [20] P. Zhao, J.C. Heinrich, and D.R. Poirier. Dendritic solidification of binary alloys with free and forced convection. *International Journal for Numerical Methods in Fluids*, 49(3):233–266, 2005.
- [21] C. Beckermann, H.-J Diepers, I. Steinbach, A. Karma, and X. Tong. Modeling melt convection in phase-field simulations of solidification. *Journal of Computational Physics*, 154(2):468 – 496, 1999.
- [22] X. Tong, C. Beckermann, A. Karma, and Q. Li. Phase-field simulations of dendritic crystal growth in a forced flow. *Phys. Rev. E*, 63:61601, 2001.
- [23] J.-H. Jeong, N. Goldenfeld, and J.A. Dantzig. Phase field model for three-dimensional dendritic growth with fluid flow. *Phys. Rev. E*, 64(041602):416021–4160214, 2001.
- [24] J.-H. Jeong, J.A. Dantzig, and N. Goldenfeld. Dendritic growth with fluid flow in pure materials. *Metall. Mater. Trans. A*, 34:459–466, 2003.
- [25] Y. Lu, C. Beckermann, and J.C. Ramirez. Three-dimensional phase-field simulations of the effect of convection on free dendritic growth. *Journal of Crystal Growth*, 280(1):320 – 334, 2005.
- [26] R. Rojas, T. Takaki, and M. Ohno. A phase-field-lattice boltzmann method for modeling motion and growth of a dendrite for binary alloy solidification in the presence of melt convection. *Journal of Computational Physics*, 298:29 – 40, 2015.
- [27] Viardn A Tourret D, Sturz L and Založnik M. Comparing mesoscopic models for dendritic growth. *IOP Conf. Ser.: Mater. Sci. Eng.*, current issue, 2020.
- [28] D. Tourret and A. Karma. Multiscale dendritic needle network model of alloy solidification. *Acta Materialia*, 61(17):6474 – 6491, 2013.
- [29] D. Tourret and A. Karma. Three-dimensional dendritic needle network model for alloy solidification. *Acta Materialia*, 120:240 – 254, 2016.
- [30] D. Tourret, A. Karma, A. J. Clarke, P. J. Gibbs, and S. D. Imhoff. Three-dimensional dendritic needle network model with application to al-cu directional solidification experiments. *IOP Conference Series: Materials Science and Engineering*, 84:012082, jun 2015.
- [31] Damien Tourret, Amy J Clarke, Seth D Imhoff, Paul J Gibbs, John W Gibbs, and Alain Karma. Three-dimensional multiscale modeling of dendritic spacing selection during al-si directional solidification. *JOM*, 67(8):1776–1785, 2015.
- [32] D. Tourret, M.M. Francois, and A.J. Clarke. Multiscale dendritic needle network model of alloy solidification with fluid flow. *Computational Materials Science*, 162:206 – 227, 2019.

- [33] T. Haxhimali, A. Karma, F. Gonzales, and M. Rappaz. Orientation selection in dendritic evolution. *Nature Materials*, 5:660 – 664, 2006.
- [34] J. A. Dantzig, P. Di Napoli, J. Friedli, and M. Rappaz. Dendritic growth morphologies in al-zn alloys-part ii: Phase-field computations. *Metallurgical And Materials Transactions A-Physical Metallurgy And Materials Science*, 44(12):5532–5543, 2013.
- [35] J.S Langer. Lectures in the theory of pattern formation (les houches, session xlv). In J. Souletie, J. Vannimenus, and R. Stora, editors, *Chance and Matter*, pages 629–711. North-Holland, New York, 1987.
- [36] J.S. Langer. Dendrites, viscous fingers, and the theory of pattern formation. *Science*, 243(4895):1150 – 1156, 1989.
- [37] A. Barbieri and J.S. Langer. Predictions of dendritic growth rates in the linearized solvability theory. *Phys. Rev. A*, 39:5314–5325, 1989.
- [38] M. Ben Amar and E. Brener. Theory of pattern selection in three-dimensional nonaxisymmetric dendritic growth. *Phys. Rev. Lett.*, 71(4):589, 1993.
- [39] A. Karma and W.-J. Rappel. Quantitative phase-field modeling of dendritic growth in two and three dimensions. *Phys. Rev. E*, 57(4):4323–4349, 1998.
- [40] N. Provatas, N. Goldenfeld, and J. Dantzig. Efficient computation of dendritic microstructures using adaptive mesh refinement. *Phys. Rev. Lett.*, 80(15):3309–3311, 1998.
- [41] M. Plapp and A. Karma. Multiscale random-walk algorithm for simulating interfacial pattern formation. *Phys. Rev. Lett.*, 84(8):1740, 2000.
- [42] P. Bouissou and P. Pelce. Effect of a forced flow on dendritic growth. *Phys. Rev. A*, 40:6673 – 6680, 1989.
- [43] C. H. K. Williamson. Defining a universal and continuous strouhalreynolds number relationship for the laminar vortex shedding of a circular cylinder. *The Physics of Fluids*, 31(10):2742–2744, 1988.
- [44] F.L. Ponta and H. Aref. Strouhal-reynolds number relationship for vortex streets. *Phys. Rev. Lett.*, 93:084501, 2004.
- [45] T. Von Krmn. *Aerodynamics: selected topics in the light of their historical development*. Dover, 2004.
- [46] C. H. K. Williamson. The existence of two stages in the transition to threedimensionality of a cylinder wake. *The Physics of Fluids*, 31(11):3165–3168, 1988.
- [47] C. H. K. Williamson. Oblique and parallel modes of vortex shedding in the wake of a circular cylinder at low reynolds numbers. *Journal of Fluid Mechanics*, 206:579627, 1989.
- [48] C. H. K. Williamson. Vortex dynamics in the cylinder wake. *Annual Review of Fluid Mechanics*, 28(1):477–539, 1996.
- [49] G.P. Ivantsov. Temperature field around a spheroidal, cylindrical and acicular crystal growing in a supercooled melt. *Dokl Akad Nauk SSSR.*, 58:567–569, 1947.
- [50] S. Sakane, T. Takaki, M. Ohno, Y. Shibuta, T. Shimokawabe, and T. Aoki. Three-dimensional morphologies of inclined equiaxed dendrites growing under forced convection by phase-field-lattice boltzmann method. *Journal of Crystal Growth*, 483:147 – 155, 2018.
- [51] A. Badillo, D. Ceynar, and C. Beckermann. Growth of equiaxed dendritic crystals settling in an undercooled melt, part 1: Tip kinetics. *Journal of Crystal Growth*, 309(2):197 – 215, 2007.
- [52] I. Steinbach. Pattern formation in constrained dendritic growth with solutal buoyancy. *Acta Materialia*, 57(9):2640 – 2645, 2009.
- [53] A. Viardin, J. Zollinger, L. Sturz, M. Apel, J. Eiken, R. Berger, and U. Hecht. Columnar dendritic solidification of tial under diffusive and hypergravity conditions investigated by phase-field simulations. *Computational Materials Science*, page 109358, 2019.
- [54] Damien Tourret and Alain Karma. Growth competition of columnar dendritic grains: A phase-field study. *Acta Materialia*, 82:64–83, 2015.
- [55] Damien Tourret, Younggil Song, Amy Jean Clarke, and Alain Karma. Grain growth competition during thin-sample directional solidification of dendritic microstructures: A phase-field study. *Acta Materialia*, 122:220–235, 2017.